Ecological Indicators 185 (2026) 114756

Contents lists available at ScienceDirect

Ecological Indicators

journal homepage: www.elsevier.com/locate/ecolind

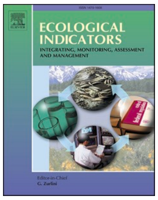

Evidence of enhanced global vegetation activity driven by reduced human pressures

Aoyang He[a], Zhijun Dai[a,b,*], Xuefei Mei[a], Jinping Cheng[c], Sergio Fagherazzi[d], Zhenzhong Zeng[e]

[a] *State Key Laboratory of Estuarine and Coastal Research, East China Normal University, Shanghai, China*
[b] *Laboratory for Marine Geology, Qingdao Marine Science and Technology Center, Qingdao, China*
[c] *Department of Science and Environmental Studies, The Education University of Hong Kong, New Territories, Hong Kong, China*
[d] *Department of Earth and Environment, Boston University, Boston, USA*
[e] *School of Environment Science and Engineering, Southern University of Science and Technology, Shenzhen, China*

ARTICLE INFO

Keywords:
COVID-19 pandemic
Vegetation dynamic
Anthropogenic pressure
Difference-in-Differences

ABSTRACT

The COVID-19 pandemic provided an unprecedented natural experiment to assess vegetation responses to reduced anthropogenic pressures. We developed a multi-scale framework synthesizing policy stringency, human mobility, and remote sensing data to quantify pandemic impacts on global vegetation. Specifically, we constructed a spatially explicit Human Modification Stringency Index to capture relative shifts in human activity from 2017 to 2023, while characterizing vegetation dynamics using Dynamic World land cover and MODIS NDVI. Our results reveal that global vegetation area, which had declined by ~2.3 million km^2 before the pandemic, rebounded with a net gain of ~2.9 million km^2 during the pandemic. This reversal was corroborated by growing-season NDVI, which transitioned from browning (−0.0021) to greening (+0.0056). Using a continuous Difference-in-Differences model across ~28.3 million pixels, we causally attributed this greening to reduced human disturbance in 96.6% of significant grid cells. The effects peaked in 2022 before diminishing as restrictions eased. Notably, moderately human-modified landscapes showed the most widespread recovery, whereas heavily modified areas exhibited the greatest magnitude of change, suggesting substantial latent vegetation recovery potential. These findings highlight that targeted reductions in anthropogenic pressures can drive rapid vegetation recovery, offering critical insights for ecological restoration and land management.

1. Introduction

Vegetation anchors terrestrial ecosystems, driving carbon sequestration and climate regulation while sustaining global biodiversity (Cortés et al., 2021; DiMiceli et al., 2021; Piao et al., 2011). Yet, human activities—coupled with intensifying droughts, wildfires, and extreme weather—have accelerated vegetation loss, threatening Earth's ecological balance (Affram et al., 2023; Chen et al., 2019; Higgins et al., 2023). Quantifying the specific impacts of anthropogenic pressures versus natural climate variability on vegetation dynamics has long been challenging, as these drivers are typically deeply intertwined and operate simultaneously. The COVID-19 pandemic, declared by the World Health Organization in March 2020, created an unprecedented natural experiment by drastically reducing human activity worldwide, offering a unique opportunity to study vegetation responses to abruptly diminished anthropogenic pressures (Dang et al., 2024; Su et al., 2021).

Throughout the COVID-19 pandemic, global lockdown measures curbed transportation, industry, and mobility, with stringent restrictions peaking in the early pandemic (EP, 2019–2021) and gradually easing in the late pandemic (LP, 2021–2023) until the pandemic's status was downgraded in May 2023 (Chen et al., 2024a; Chinazzi et al., 2020; Lenharo, 2023). Regional studies during the EP reported significant ecological benefits, such as an 8.4-day earlier spring onset in China and enhanced vegetation greenness in India, linked to reduced human disturbances and improved air quality (Kashyap et al., 2023; Su et al., 2021). However, a comprehensive global assessment comparing the baseline before the pandemic (BP, 2017–2019) with the entire pandemic period is still lacking, particularly one that employs a framework capable of rigorously decoupling localized, patchy human disturbances from broad, gradual climate variability to isolate the net effects of

---

[*] Corresponding author at: State Key Laboratory of Estuarine and Coastal Research, East China Normal University, Shanghai, China.
E-mail address: zjdai@sklec.ecnu.edu.cn (Z. Dai).

https://doi.org/10.1016/j.ecolind.2026.114756
Received 24 November 2025; Received in revised form 3 March 2026; Accepted 3 March 2026

restrictions.

In this study, we developed a multi-scale analytical framework integrating policy restrictions, human mobility, and remote sensing datasets, to quantify the spatiotemporal impact of human activity restrictions on global vegetation. We constructed a Human Modification Stringency Index (HMSI) by fusing the government response Stringency Index (SI) with the global Human Modification (HM) to spatially resolve the intensity of pandemic-induced activity reductions. Vegetation dynamics were characterized using Dynamic World (DW) land cover data for area mapping and MODIS NDVI for assessing vegetation activity. Our analytical framework progressed from examining macro-scale correlations between national human mobility trends and vegetation area to a local-scale causal identification. Utilizing a continuous Difference-in-Differences (DID) model, we leveraged the HMSI to isolate the net causal effect of pandemic-induced human activity restrictions on vegetation activity, effectively disentangling anthropogenic impacts from confounding climatic drivers.

2. Materials and methods

2.1. *Quantifying spatiotemporal human activity restrictions*

We combined datasets on policy restrictions, human mobility, and human modification to quantify the COVID-19 pandemic's impact on human activity. Policy restrictions were measured using the SI from the Oxford Coronavirus Government Response Tracker (OxCGRT) (Hasell et al., 2020). The SI aggregates nine policy indicators (e.g., school and workplace closures, travel bans) into a normalized 0–1 scale (Hale et al., 2021). Human mobility changes were assessed using Google COVID-19 Community Mobility Reports (CMR), which track the number of visitors to public transport stations (TS) and time spent at home (AH) as percentage deviations from a pre-pandemic baseline (January 3–February 6, 2020) (Sulyok and Walker, 2020; Mathieu et al., 2020).

To spatially resolve pandemic-induced human activity reductions, we developed the HMSI by fusing the temporally varying SI (national scale, 2020–2022) with the static global HM (gHM) dataset. The HM characterizes baseline anthropogenic pressure at 1 km resolution on a 0–1 scale, incorporating five major stressors including human settlement and transportation infrastructure (Kennedy et al., 2019). The HMSI was computed as:

$$HMSI_{i,t} = HM_i \times SI_{j,t} \tag{1}$$

where HM_i is the baseline human modification at grid cell i, $SI_{j,t}$ is the annual mean SI for country j in year t (2020–2022), with 2019 and 2023 defined as 0 to denote the absence of restrictions during the pre-pandemic baseline and the recovery period. The multiplicative formulation captures the interaction between pre-existing anthropogenic pressure, which defines the magnitude of activity susceptible to restriction, and policy stringency, which modulates the degree of curtailment. High HMSI values thus pinpoint locations where intensive human activity coincided with stringent restrictions, whereas locations with minimal baseline footprint yield near-zero values regardless of policy stringency, reflecting limited scope for further reduction.

2.2. *Mapping global vegetation activity and dynamics*

Global vegetation distribution was mapped using the 10 m resolution Dynamic World (DW) dataset derived from Sentinel-2 imagery (Brown et al., 2022). Annual mode composites were generated in Google Earth Engine by assigning pixels their most frequent class. To prioritize high-confidence detection over categorical precision, we aggregated trees, shrubs, grass, and flooded vegetation into a binary vegetation metric (Table S1). This approach effectively mitigates confusion among spectrally similar vegetation types while simplifying structural details.

The analysis was restricted to continental areas between 55°S and 70°N to minimize high-latitude atmospheric interference (e.g., clouds, snow). Sparsely populated polar regions were excluded as they experienced limited anthropogenic pressure during the pandemic. Following Olofsson et al. (2014), we derived unbiased area estimates (A) and standard errors (SE) using a simplified binary vegetation error matrix (Table S2). Uncertainty in net area change (ΔA) was estimated by propagating errors under the assumption of temporal independence:

$$\mathrm{SE}(\Delta A) = \sqrt{SE_i^{\,2} + SE_j^{\,2}} \tag{2}$$

with 95% confidence intervals constructed as ΔA±1.96×SE(ΔA). We note that uncertainties for gross gain and loss flows could not be rigorously quantified in the absence of temporally paired validation samples capturing specific transitions.

We quantified changes in vegetation cover at both global and regional scales before and during the pandemic across various time periods and vegetation categories. The percentage change in vegetation within each 1° grid cell was calculated using the following formula:

$$P_{i,j} = \frac{IA_{i,j} - DA_{i,j}}{TA_{i,j}} \times 100\% \tag{3}$$

where i and j denote the start and end years; $IA_{i,j}$ and $DA_{i,j}$ represent vegetation gain and loss areas, respectively; and $TA_{i,j}$ is the total grid cell area. Positive and negative values indicate net vegetation increase and decrease, respectively. To characterize the spatial intensity of change, we further tallied the number of 1° grid cells exceeding specified change thresholds:

$$G_p = \sum \left[\left| P_{i,j} \right| \geq p\% \right] \tag{4}$$

where G_p represents the number of 1° grid cells with vegetation change greater than or equal to p percent, evaluated at thresholds of 10%, 20%, 30%, 40%, 50%, and 60%.

Vegetation activity was quantified using the Normalized Difference Vegetation Index (NDVI) derived from the MOD13A2 V6.1 product (Didan, 2021). To account for latitudinal variations in phenology, the growing-season mean NDVI ($\mathrm{NDVI_{GS}}$) was computed according to climatic October for the Northern Hemisphere extratropics, October–April (spanning two calendar years) for the Southern Hemisphere extratropics, and the full annual cycle for the tropics. $\mathrm{NDVI_{GS}}$ values were calculated for each pixel over the period 2017–2023. To ensure the analysis focused on vegetated regions, pixels with a mean annual NDVI below 0.2 were excluded, thereby masking barren land, water bodies, and permanent snow or ice.

Trends in $\mathrm{NDVI_{GS}}$ were analyzed across three distinct periods (BP, EP, and LP) to assess shifts in vegetation activity before and during the pandemic. Crucially, $\mathrm{NDVI_{GS}}$ served as the primary response variable for evaluating the net impact of pandemic-related restrictions on vegetation dynamics, offering a continuous, physiologically meaningful metric to complement the categorical vegetation cover analysis.

2.3. *Macro-scale correlation and local-scale causal identification of human activity restrictions on vegetation*

Our analytical framework progresses from macro-scale correlations to local-scale causal inference. We first examined national-scale associations between human mobility changes and vegetation dynamics during the COVID-19 pandemic. We focused on Australia, Canada, Russia, and India due to their large landmasses, rich vegetation, and broad latitudinal spans. Through correlation analyses of SI, TS, and AH, and a comparison of vegetation trends against human mobility, we aimed to investigate whether pandemic-induced reductions in human activity were linked to measurable national-scale vegetation changes.

National-scale correlations cannot effectively disentangle anthropogenic effects from confounding climatic drivers. To isolate the causal impact of reduced human disturbance on vegetation, we employed a continuous DID model (Callaway et al., 2024) treating the COVID-19 pandemic as a quasi-natural experiment. Our identification strategy exploits the spatial mismatch between broad, gradual climatic forcing and localized, abrupt anthropogenic disturbance. Within 0.5° grid cells, we assume sub-grid pixels (1 km × 1 km) share identical climatic conditions; thus, variation in human modification intensity across pixels provides the necessary contrast for causal inference. We estimated the following two-way fixed effects model:

$$NDVI_{i,t} = \beta \times HMSI_{i,t} + \mu_i + \lambda_t + \varepsilon_{i,t} \tag{5}$$

where $NDVI_{i,t}$ is the $NDVI_{GS}$ for pixel i in year t; $HMSI_{i,t}$ is the continuous treatment variable capturing the intensity of human activity restriction. The pixel fixed effect μ_i absorbs all time-invariant spatial characteristics (e.g., topography, soil type, vegetation type, and baseline human modification), while the year fixed effect λ_t absorbs all spatially invariant temporal shocks (e.g., large-scale climatic anomalies and macro-level policy trends). Accordingly, β isolates the net effect of human activity restriction on vegetation activity, controlling for both static spatial and dynamic temporal confounders.

Given that vegetation sensitivity to reduced disturbance varies with baseline anthropogenic pressure, we stratified pixels into low, medium, and high groups based on initial human modification and estimated models separately for each. The models were estimated using a within-transformation to eliminate fixed effects, followed by Ordinary Least Squares (OLS) regression with cluster-robust standard errors. Grid cells were retained if at least one sub-group yielded a statistically significant estimate ($p < 0.05, R^2 \geq 0$). To further validate the causal interpretation, we conducted a pooled event study analysis by aggregating all validated pixels into a single panel with two-way fixed effects. By controlling for global covariate shocks, such as El Niño–Southern Oscillation (ENSO) events, we analyzed the causal relationship between human activity restrictions and vegetation recovery.

3. Results

3.1. Global vegetation trends before and during the COVID-19 pandemic

We analyzed vegetation area dynamics across 1° grid cells, employing bias-corrected estimates to address map classification uncertainties. The analysis highlights a general decreasing trend in global vegetation area during the BP, followed by substantial recovery in the EP and LP (Fig. 1). Vegetation losses during the BP were concentrated in the Northern Hemisphere (40–70°N) and southern mid-latitudes

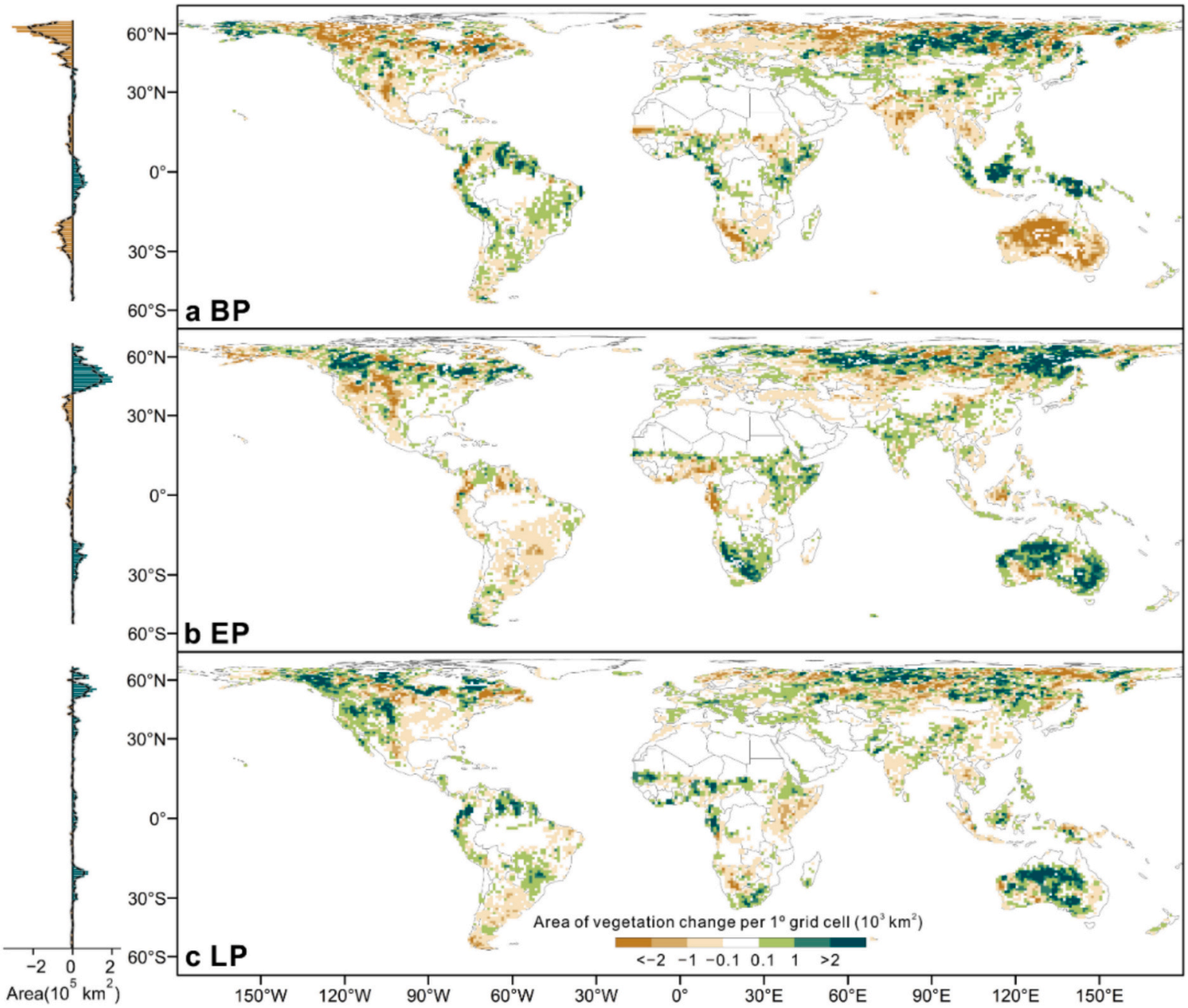

Fig. 1. Global vegetation area changes before and during the COVID-19 pandemic for (a) BP (2017–2019), (b) EP (2019–2021), and (c) LP (2021–2023). Vegetation area changes are depicted in km^2 per 1° grid cell. The colors brown and green indicate a decrease and an increase of vegetation, respectively, with the colour darkness indicating the magnitude of change. The left panels show latitudinal summaries of net vegetation change, the dashed lines represent the unbiased area estimates, and the gray shading indicates the 95% confidence intervals. (For interpretation of the references to colour in this figure legend, the reader is referred to the web version of this article.)

(20–40°S). During the EP, these zones experienced a pronounced reversal, driving net global expansion (Fig. 1b; Table S4). In the LP, however, the magnitude of high-latitude expansion attenuated, while tropical regions (20°S–20°N) transitioned from net loss during the EP to significant net gain (Fig. 1c; Table S4). Quantitatively, the global adjusted net vegetation area decreased by approximately 2,254,532 km^2 during the BP, whereas the EP witnessed a substantial net rebound of 1,647,244 km^2 (95% CI: 1,596,814–1,697,675 km^2), and the LP sustained a further net gain of 1,244,690 km^2 (95% CI: 1,194,419–1,294,962 km^2). Cumulatively, bias-corrected estimates indicate a total net vegetation gain of approximately 2.9 million km^2 during the pandemic periods, substantially offsetting pre-pandemic losses.

These global trends were unevenly distributed across regions (Fig. 2a–d; Table S5). Europe and Russia exhibited the largest gain of ~1,322,000 km^2 during the EP (Fig. 2a; Table S3), with EP gains exceeding those of the LP. In North America, the LP contribution surpassed that of the EP, yielding a net gain of ~584,000 km^2 (Fig. 2b). Sub-Saharan Africa showed stronger recovery during the EP, with a net gain of ~193,000 km^2 (Fig. 2d). Oceania experienced vegetation increases during both phases, with net gains of ~429,000 km^2 and ~338,000 km^2 in the EP and LP, respectively (Fig. 2c). Conversely, the Middle East and South Asia exhibited relatively modest changes (Fig. S2d–e), while Latin America and Southeast Asia experienced net losses of ~158,000 km^2 and ~54,000 km^2, respectively (Fig. S2a, c; Table S3). Among vegetation types, tree forests were the most responsive, with notable increases in Europe and Russia (24.2%) and North America (9.6%) during the EP (Table S3; Fig. S4f). Shrubs reversed pre-pandemic declines in Oceania, with net gains of ~341,000 km^2 and ~205,000 km^2 during the EP and LP, respectively (Fig. S3c), while North America experienced a 15.1% increase in shrub coverage (Table S3; Fig. S3b). Sub-Saharan Africa and Oceania were the only regions recording net grassland gains. Flooded vegetation, despite covering the smallest area globally, increased during the pandemic with a net gain of ~28,000 km^2 during the EP. Conversely, grasslands experienced accelerated losses during the EP, with only partial recovery in the LP (Table S3).

Complementing area-based changes, NDVI$_{GS}$ revealed finer-scale vegetation dynamics across the three phases (Fig. 3). The BP was characterized by broadly suppressed vegetation activity, as evidenced by a probability density distribution of NDVI changes (ΔNDVI) with a negative mean of −0.0021 (Fig. 3a). Extensive browning occurred in Australia and southern Africa, contrasting with scattered greening in eastern North America and East Asia. This trend reversed sharply during the EP, where the global mean ΔNDVI peaked at 0.0056, indicating enhanced productivity (Fig. 3b). Widespread greening was evident in eastern Australia, the Indian subcontinent and southern Africa. During the LP, the mean ΔNDVI declined to a near-neutral value of 0.0002, suggesting a return toward equilibrium (Fig. 3c).

3.2. *Spatiotemporal associations between human activity and vegetation dynamics*

The COVID-19 pandemic imposed significant constraints on human activities (Diffenbaugh et al., 2020; Manica et al., 2021), evidenced by a strong negative correlation between the TS and SI, while AH showed a positive correlation with SI ($P < 0.001$; Fig. 4). These relationships were more pronounced in the EP compared to LP, as indicated by steeper regression slopes in the EP.

The stricter restrictions on human activities associated with higher SI levels led to increased AH and decreased TS, accompanied by significant vegetation increase (Fig. 5). Australia and Canada showed synchronous patterns between human activity and vegetation dynamics in both the EP and LP (Fig. 5a, b). However, in Russia and India, relaxed restrictions in the LP caused a marked increase in TS, stalling vegetation expansion (Fig. 5c, d). In India, this TS increase implies that urban food shortages drove reverse migration to rural regions, leading to rural vegetation loss (Fakir and Bharati, 2021; Roy and Agarwal, 2020). Collectively, the spatiotemporal consistency between reduced human mobility and vegetation anomalies indicates a potential association between human activity and global vegetation changes.

3.3. *Net greening effects derived from restricted human activity*

We utilized a continuous DID model within 0.5° grid cells to disentangle anthropogenic impacts from climatic variability. The analysis

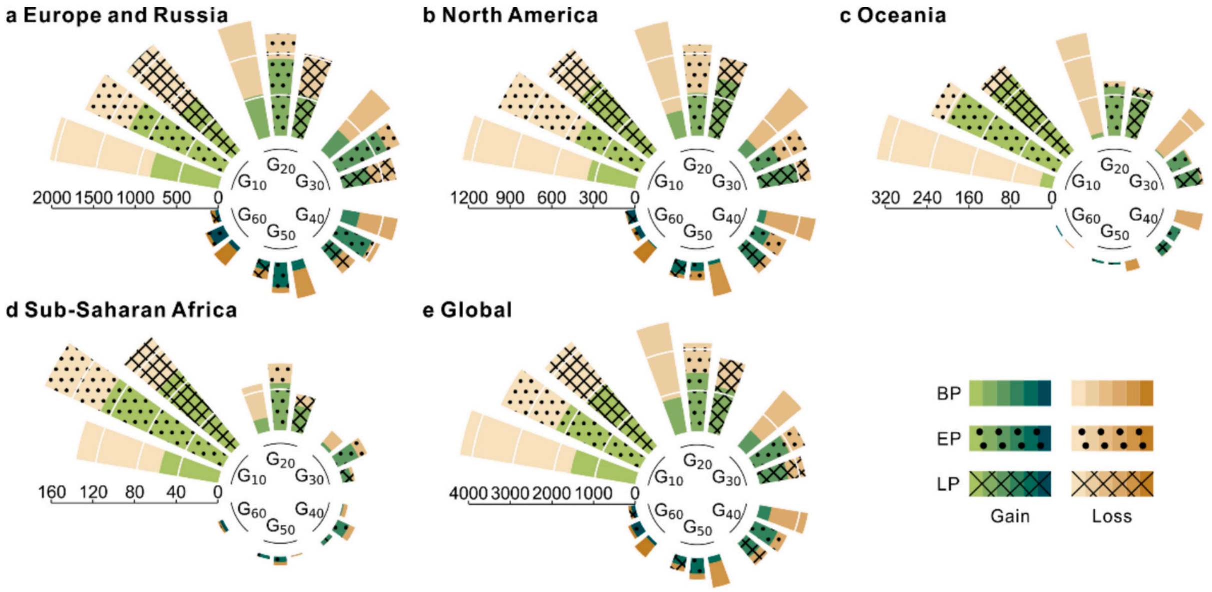

Fig. 2. One-degree grid cells exhibiting varying magnitudes of vegetation change before and during the COVID-19 pandemic. The panels depict vegetation losses and gains for (**a**) North America, (**b**) Europe and Russia, (**c**) Oceania, (**d**) Sub-Saharan Africa, and (**e**) the global study area, across the periods of BP, EP, and LP. Categories G_{10}, G_{20}, G_{30}, G_{40}, G_{50}, and G_{60} represent the number of 1° grid cells with vegetation change greater than or equal to 10%, 20%, 30%, 40%, 50%, and 60%, respectively. Brown indicates vegetation loss, while green denotes vegetation gain. Blank, dotted, and striped patterns correspond to the periods of BP, EP, and LP. (For interpretation of the references to colour in this figure legend, the reader is referred to the web version of this article.)

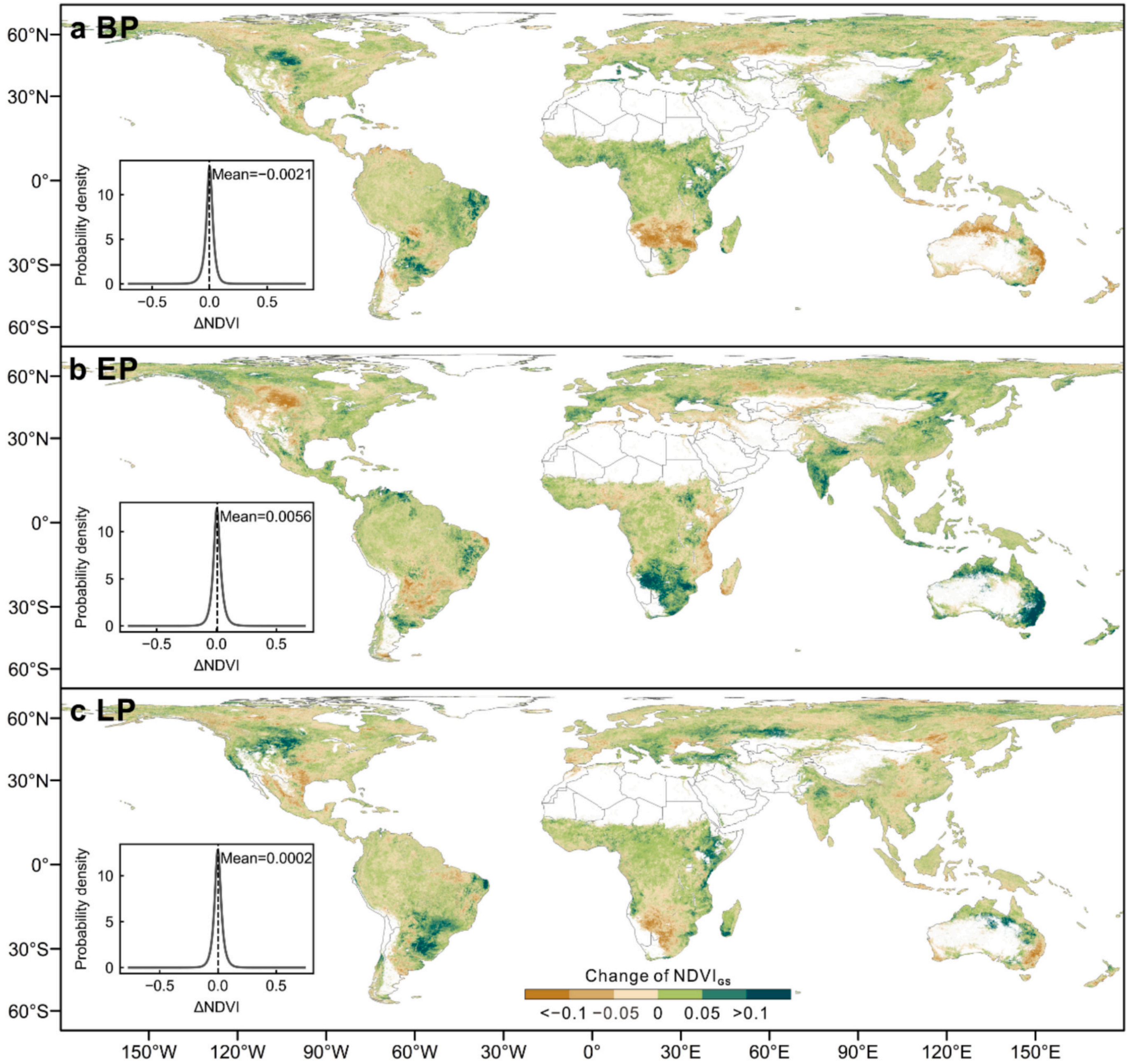

Fig. 3. Global trends in vegetation NDVI before and during the COVID-19 pandemic for (a) BP (2017–2019), (b) EP (2019–2021), and (c) LP (2021–2023). Changes in NDVI_{GS} are shown at 1 km resolution. The colors brown and green indicate a decrease and an increase of NDVI, respectively, with the colour darkness indicating the magnitude of change. Lower-left insets present probability density distributions and mean values of NDVI changes (ΔNDVI). (For interpretation of the references to colour in this figure legend, the reader is referred to the web version of this article.)

indicates a widespread positive vegetation response to pandemic-related restrictions. Among the grid cells demonstrating model robustness ($R^2 \geq 0$) and statistical significance ($p < 0.05$), 96.6% exhibited a positive net effect (Fig. 6a). The mean regression coefficient of 0.0176 confirms that reduced human activity generally mitigated vegetation stress.

However, the magnitude and prevalence of this recovery varied non-monotonically with baseline HM intensity (Figs. 6b–c, S5). Medium HM areas demonstrated the most consistent response, accounting for the highest proportion of statistically significant grid cells (50.4%) with a moderate mean coefficient of 0.0177. In contrast, High HM areas displayed a pattern of localized but intense effects. Despite significance appearing in only 10.0% of cells, the mean coefficient (0.0346) was nearly double that of the medium group, underscoring a strong potential for vegetation rebound. Low HM areas showed intermediate results, with 19.2% significance and a mean coefficient of 0.0194. Consequently, while vegetation recovery is most prevalent in semi-modified landscapes, its magnitude is greatest in heavily modified environments where latent recovery potential is unlocked by the cessation of intense activity.

To validate the causal interpretation of these spatial patterns, we conducted a pooled event study using an extensive panel dataset of ~28.3 million pixels spanning seven years (Fig. 6d). The estimated coefficients show no pre-treatment trend before the pandemic, with a mean of 0.012, fulfilling a critical condition for identification. Following the onset of disruption in 2020, a positive effect intensified to a peak of 0.030 in 2022, aligning with the time lags required for vegetation growth. Subsequently, the coefficient dropped to 0.010 in 2023 as human mobility recovered. This decline serves as a validation test,

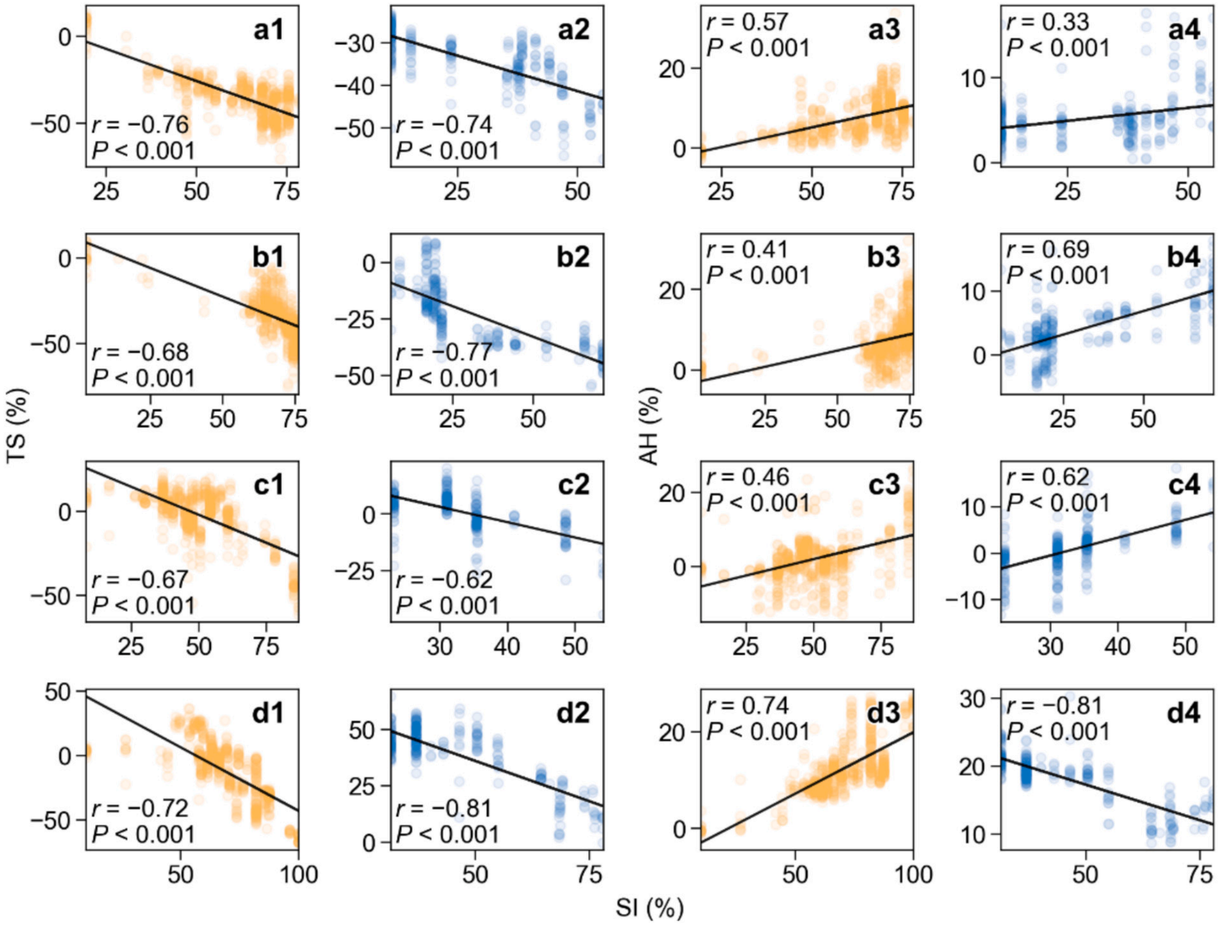

Fig. 4. Scatter plots of correlation between the government response stringency index (SI) and the changes in human activities, including the number of visitors to public transport stations (TS) and the time spent at home (AH) in EP and LP. Panels show correlation relationships between TS and SI during EP (**a–d1**), and LP (**a–d2**), as well as correlations between AH and SI during EP (**a–d3**), and LP (**a–d4**) for Australia (**a1–4**), Canada (**b1–4**), Russia (**c1–4**) and India (**d1–4**). TS and AH represent changes relative to baseline days, defined as the median value from January 3 to February 6, 2020. Orange and blue dots indicate EP and LP periods, respectively. Solid lines represent correlation relationships, with fit statistics (*r* and *P* values) included. (For interpretation of the references to colour in this figure legend, the reader is referred to the web version of this article.)

confirming that the greening phenomenon was contingent upon the reduction in human activity.

4. Discussion

4.1. Vegetation recovery patterns driven by reduced anthropogenic pressures

We identified significant shifts in global surface vegetation patterns linked to COVID-19 containment measures. The reduction in human activity triggered a widespread increase in vegetation coverage, particularly in Australia, Canada, and Russia (Fig. 5a–c). These findings are consistent with the recent rebound in global-mean $NDVI_{GS,}$ which shifted from persistently low values in 2018–2019 to a sharp rise during 2020–2023 (Li et al., 2024), a trend mirrored by the consistency between vegetation area and NDVI shown in Figs.1 and 3. Our results suggest that this recovery was not driven solely by climatic factors but by the dramatic decline in anthropogenic disturbances. Lockdowns reduced direct physical damage to vegetation while indirectly enhancing atmospheric clarity and canopy radiation (Dang et al., 2024; Kashyap et al., 2023), collectively driving abrupt vegetation growth. However, regional variations in recovery extent and timing persisted, reflecting differences in national containment strategies.

Furthermore, our continuous DID analysis revealed a non-monotonic relationship between baseline HM intensity and pandemic-induced ecological rebound (Figs. 6b–c, S5). Semi-modified landscapes (medium HM) exhibited the highest vegetation recovery prevalence. In these regions, sufficient ecological integrity remained to support widespread greening once anthropogenic pressures subsided, despite prior suppression (Fig. S6c–d; Table S6). Conversely, high HM areas showed low prevalence but the greatest magnitude. While infrastructure limits physical space and signal detectability in these zones (Smith et al., 2022; Zhu et al., 2016), the exceptional magnitude of detected changes suggests substantial, albeit spatially constrained, latent vegetation recovery potential. Low HM areas showed intermediate results, with greening driven by reduced extraction and fire in forests (Fig. S7), yet limited by harsh conditions in arid zones (Fig. S2e).

4.2. Disentangling natural and anthropogenic drivers of vegetation change

By employing a continuous DID model, we successfully isolated the causal effects of human disturbance from the background noise of climatic variability. While statistically significant associations between reduced human activity and vegetation dynamics were detected in 28.3% of the analyzed grids, the remaining grids did not exhibit a significant response to human activity restrictions. In these areas, the potential benefits of reduced human activity were overshadowed by large-scale climatic extremes, which emerged as the dominant factors suppressing vegetation growth (Boer et al., 2020; Gomes et al., 2021). During the EP, shrubs and grasses recorded losses of ~130,000 km^2 and

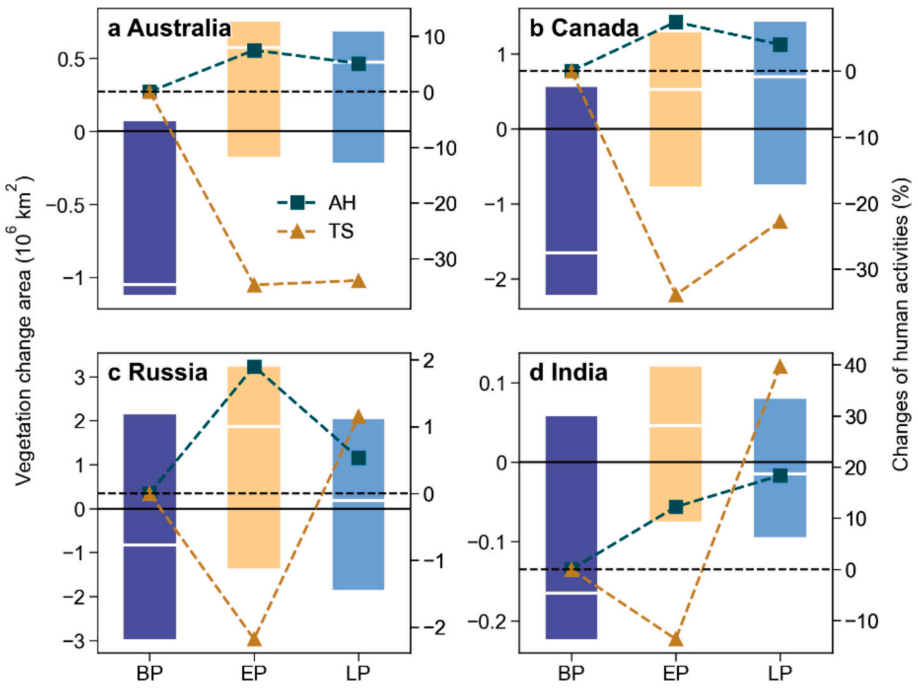

Fig. 5. Relationship between vegetation changes and human activities. The bar charts (left primary axis) show the area of vegetation change, with the white line indicating the net change. The line charts (right secondary axis) display changes in human activities for (**a**) Australia, (**b**) Canada, (**c**) Russia, and (**d**) India. The public transport stations (TS) and time spent at home (AH) represent changes relative to baseline days, defined as the median value from January 3 to February 6, 2020. Note that changes in human activities during BP are rescaled to zero as a baseline for comparison during EP and LP.

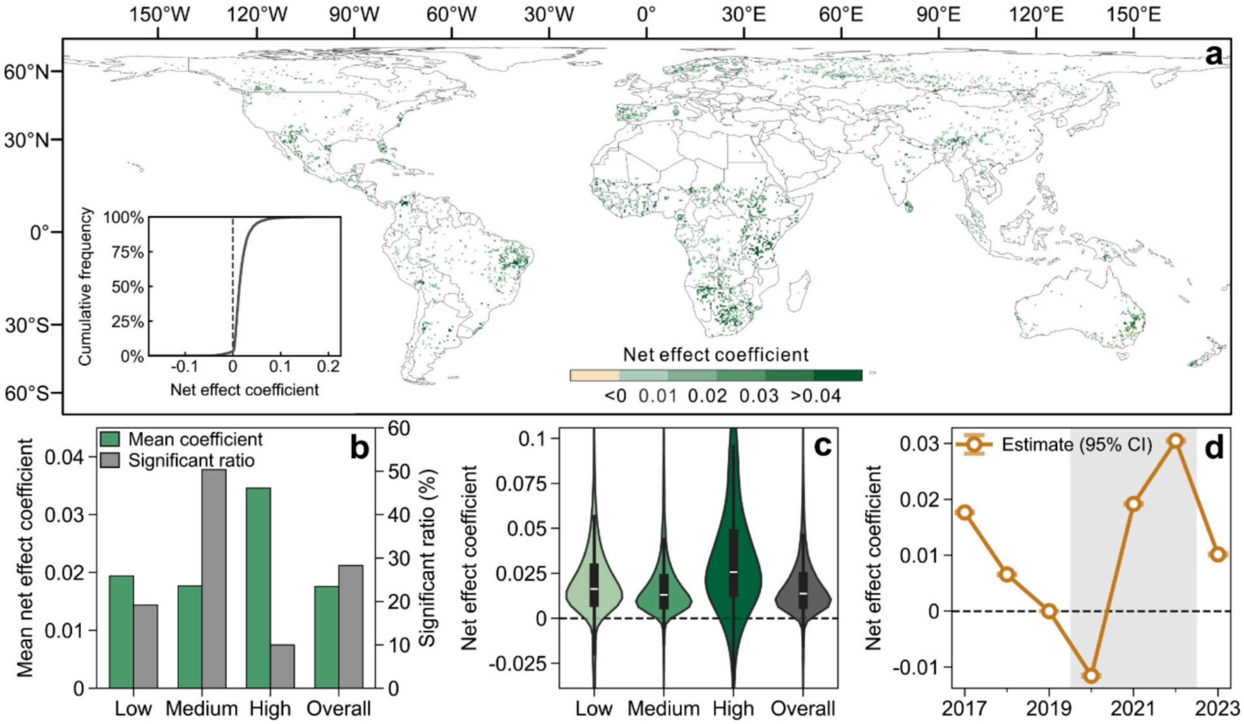

Fig. 6. Global spatial distribution and statistical characteristics of the impact of human activity restrictions on vegetation. (**a**) Global map of mean net effect coefficients for 0.5°grid cells containing at least one significant sub-group ($p < 0.05$, $R^2 \geq 0$), stratified by initial human modification (HM) intensity. The colour scale indicates the effect direction, with green shades denoting positive responses and brown shades denoting negative ones. The inset illustrates the cumulative frequency distribution of the net effect coefficients. (**b**) Statistics across restriction intensity groups (Low, Medium, High) and the Overall level. Green bars represent the mean net effect coefficient, and gray bars represent the percentage of pixels with significant effects. (**c**) Violin plots displaying the distribution of net effect coefficients for each intensity group. (**d**) Temporal dynamics of the net effect coefficient relative to the base year (2019). Points and the line track the estimates over time, with error bars representing 95% confidence intervals. The gray shaded region indicates the period following the onset of restrictions (2020–2022). (For interpretation of the references to colour in this figure legend, the reader is referred to the web version of this article.)

~133,000 km^2, respectively (Table S3; Fig. S4d), reflecting their vulnerability to droughts and heatwaves (Jiao et al., 2021; Zhang et al., 2022). In the western United States and southern Brazil, prolonged heatwaves and drought precipitated widespread vegetation dieback (Affram et al., 2023; Gomes et al., 2021) (Fig. S6d–e, Fig. S8A). Similarly, Australia's catastrophic vegetation losses in BP align with the 2019–2020 "Black Summer" wildfires (Fig. S6f), during which over 80,000 km^2 of vegetation was lost (Godfree et al., 2021).

Beyond climatic constraints, certain regions also faced intensified anthropogenic pressures that persisted despite global mobility restrictions. Unlike the general trend of reduced disturbance, these areas suffered from continued deforestation and conflict-driven degradation (Fig. S8B–C). Examples include biodiversity loss and pollution in Middle Eastern conflict zones, desertification risks exacerbated by the Israel-Palestine conflict, and unchecked deforestation in the Brazilian Amazon (Holail et al., 2024; Kaplan et al., 2022; Silva Junior et al., 2020). Additionally, socioeconomic necessities continued to drive land conversion, such as population-driven forest clearance in India and agricultural shifts resulting from the Russia-Ukraine conflict, effectively neutralizing any potential for vegetation recovery (Chen et al., 2024b; Saxena et al., 2021).

Finally, the case of China presents a unique paradox involving the interplay between policy-driven ecological engineering and natural recovery. Although China is noted for substantial pre-pandemic afforestation (Song et al., 2025), the strict lockdown policies halted these artificial greening programs, resulting in apparent stagnation in aggregate vegetation growth (Fig. S9a–c). Yet, this pause in active management masked a strong underlying natural vegetation recovery. When the absence of artificial planting was accounted for, natural vegetation growth was found to increase by approximately 95% and 66% during the EP and LP periods, respectively, relative to BP levels (Fig. S9d).

4.3. Limitations

The DW dataset provided comprehensive Sentinel-2 coverage and class-specific probability scores, making it uniquely suited for assessing vegetation dynamics compared to static LULC products (Brown et al., 2022; Venter et al., 2022). However, it exhibited certain limitations, including misclassification of low-stature or patchy vegetation and potential underestimation of urban grassland and flooded vegetation due to image quality constraints. Although agricultural lands were excluded to focus on natural recovery, vegetation changes induced by artificial greening programs could not be fully disentangled from natural resurgence. For instance, China's extensive pre-existing greening infrastructure obscured natural recovery trends until these anthropogenic contributions were removed (Fig. S9). Additionally, vegetation area estimates were based on binary vegetation/non-vegetation classification without error correction for individual vegetation types. We merely provide confidence intervals for net area changes, due to the lack of temporally paired validation samples capturing specific land cover transitions.

While the Google CMR offer valuable temporal insights into human activity changes, the dataset is subject to inherent sampling biases rooted in its data collection methodology. Since the data relies exclusively on opt-in smartphone users, it inevitably reflects disparities in smartphone penetration and internet accessibility. These biases are particularly pronounced in rural, remote, or lower-income regions, where digital connectivity is lower, potentially leading to underrepresentation of these demographics. Recognizing that such spatial heterogeneity could introduce significant noise and skew local-level analyses, we conservatively restricted the use of CMR data to correlations at the national scale, where aggregated trends remain statistically representative.

To address the resulting lack of fine-scale spatial granularity and mitigate coverage gaps, we developed the HMSI. By integrating baseline human modification layers with dynamic policy stringency data, the HMSI provides a relatively robust, spatially explicit proxy for human pressure at a high resolution. However, it is important to acknowledge that the multiplicative construction of the index (HM × SI) relies on simplifying assumptions regarding the relationship between baseline human modification and activity reduction, implicitly assuming a proportional and monotonic interaction between the two components. The HMSI should therefore be interpreted as a conceptual and parsimonious proxy of relative human pressure change rather than a direct measurement of absolute anthropogenic disturbance.

We utilized the COVID-19 shock as a quasi-natural experiment to estimate the causal impact of diminished anthropogenic activity on vegetation, employing a continuous DID approach. Although we attempted to account for varying vegetation sensitivity by stratifying pixels into low, medium, and high baseline anthropogenic pressure groups, the analysis exposed a critical methodological constraint of the continuous DID framework. While the inclusion of two-way fixed effects is standard for controlling spatiotemporal heterogeneity, it proved incompatible with the data structure in highly urbanized zones. In high-intensity HM groups, the temporal stability of the SI failed to provide sufficient variation distinct from time trends, triggering severe multicollinearity with time fixed effects. This inherent limitation of the DID estimator necessitated the exclusion of approximately 68% of the high-intensity group samples, thereby compromising the model's applicability in areas with stable anthropogenic disturbances.

5. Conclusions

This study provides comprehensive evidence that the unprecedented reduction in human activity during the COVID-19 pandemic drove a significant and measurable recovery in global vegetation. By developing a multi-scale analytical framework that integrates policy stringency, human mobility, and high-resolution remote sensing data, we quantified vegetation responses across spatial scales and rigorously disentangled anthropogenic from climatic drivers.

Our analysis demonstrates a striking reversal from pre-pandemic vegetation decline to pandemic-era recovery. The global vegetation area, which had decreased by approximately 2.3 million km^2 before the pandemic, rebounded with cumulative net gains of approximately 2.9 million km^2 during the pandemic. This recovery was corroborated by NDVI-based vegetation activity, which shifted from broad-scale browning before the pandemic to widespread greening during the early pandemic phase. Regionally, the strongest recoveries occurred in Europe, Russia, Oceania, and North America, driven primarily by increases in tree cover and shrublands, while regions affected by persistent deforestation, armed conflict, or severe climatic extremes showed limited or negative responses.

The continuous DID model provided causal evidence that reduced human disturbance was a principal driver of the observed vegetation recovery. Among statistically significant grid cells, 96.6% exhibited positive net effects, with the pooled event study confirming no pre-treatment trends and a clear intensification of greening that peaked during the restriction period before declining as human mobility recovered. This temporal pattern validates the causal link between diminished anthropogenic pressure and enhanced vegetation activity. The non-monotonic relationship between baseline human modification intensity and recovery magnitude further reveals that while semi-modified landscapes respond most consistently, heavily modified areas harbor the greatest latent potential for ecological rebound when disturbances are curtailed.

Our findings carry important implications for environmental policy and land management. They demonstrate that even temporary reductions in anthropogenic pressures can trigger rapid and substantial vegetation recovery, suggesting that targeted, spatially informed interventions in ecologically sensitive or degraded zones could yield significant ecological benefits. However, persistent vegetation losses in climatically stressed and conflict-affected regions underscore that reduced human disturbance alone is insufficient; effective restoration requires integrated strategies addressing both anthropogenic and climatic stressors simultaneously. Future research should examine the long-term sustainability of pandemic-era vegetation gains and develop adaptive management frameworks balancing socioeconomic needs with ecological conservation.

CRediT authorship contribution statement

Aoyang He: Writing – original draft, Visualization, Methodology, Formal analysis, Data curation. **Zhijun Dai:** Writing – review & editing, Supervision, Project administration, Funding acquisition, Conceptualization. **Xuefei Mei:** Writing – review & editing, Validation, Methodology. **Jinping Cheng:** Writing – review & editing, Validation, Resources. **Sergio Fagherazzi:** Writing – review & editing, Validation, Funding acquisition. **Zhenzhong Zeng:** Writing – review & editing, Validation, Resources.

Declaration of competing interest

The authors declare that they have no known competing financial interests or personal relationships that could have appeared to influence the work reported in this paper.

Acknowledgements

This research was supported by the National Natural Science Key Foundation of China (NSFC) (42430406), National Key Research and Development Program of China (2023YFE0121200), and Shanghai International Science and Technology Cooperation Fund Project (23230713800, 24230740100); S. F. was partly funded by the USA National Science Foundation awards 2224608 (PIE LTER), 1832221 (VCR LTER).

Appendix A. Supplementary data

Supplementary data to this article can be found online at https://doi.org/10.1016/j.ecolind.2026.114756.

Data availability

The Dynamic World (DW) near real-time global 10 m land use/land cover dataset was accessed via the Google Earth Engine Image Collection (https://developers.google.com/earth-engine/datasets/catalog/GOOGLE_DYNAMICWORLD_V1) (Brown et al., 2022). The growing-season Normalized Difference Vegetation Index (NDVIGS) was derived from the MOD13A2 V6.1 product (https://developers.google.com/earth-engine/datasets/catalog/MODIS_061_MOD13A2) (Didan, 2021). COVID-19 pandemic data were sourced from Our World in Data (https://github.com/owid/covid-19-data) (Hasell et al., 2020). Human mobility metrics were derived from Google COVID-19 Community Mobility Reports (https://www.google.com/covid19/mobility). The global Human Modification dataset (gHM) was accessed via Google Earth Engine (https://developers.google.com/earth-engine/datasets/catalog/CSP_HM_GlobalHumanModification) (Kennedy et al., 2019). The Fire Radiative Power (FRP) dataset was accessed from MODIS/Terra and Aqua Fire Radiative Power Data (https://modis.gsfc.nasa.gov/data/dataprod/mod14.php). Regional definitions and mapping utilized Natural Earth vector data (https://www.naturalearthdata.com/downloads/110m-cultural-vectors).

References

Affram, G., Zhang, W., Hipps, L., Ratterman, C., 2023. Characterizing the development and drivers of 2021 Western US drought. Environ. Res. Lett. 18, 044040. https://doi.org/10.1088/1748-9326/acc95d.

Boer, M.M., Resco de Dios, V., Bradstock, R.A., 2020. Unprecedented burn area of Australian mega forest fires. Nat. Clim. Chang. 10, 171–172. https://doi.org/10.1038/s41558-020-0716-1.

Brown, C.F., Brumby, S.P., Guzder-Williams, B., Birch, T., Hyde, S.B., Mazzariello, J., Czerwinski, W., Pasquarella, V.J., Haertel, R., Ilyushchenko, S., Schwehr, K., Weisse, M., Stolle, F., Hanson, C., Guinan, O., Moore, R., Tait, A.M., 2022. Dynamic World, near real-time global 10 m land use land cover mapping. Sci. Data 9, 1–17. https://doi.org/10.1038/s41597-022-01307-4.

Callaway, B., Goodman-Bacon, A., Sant'Anna, P., 2024. Difference-in-Differences with a continuous treatment. NBER Working Paper No. w32117. Available at SSRN: https://ssrn.com/abstract=4716682.

Chen, C., Park, T., Wang, X., Piao, S., Xu, B., Chaturvedi, R.K., Fuchs, R., Brovkin, V., Ciais, P., Fensholt, R., Tømmervik, H., Bala, G., Zhu, Z., Nemani, R.R., Myneni, R.B., 2019. China and India lead in greening of the world through land-use management. Nat. Sustainability 2, 122–129. https://doi.org/10.1038/s41893-019-0220-7.

Chen, Z., Tsui, J.L.-H., Gutierrez, B., Busch Moreno, S., du Plessis, L., Deng, X., Cai, J., Bajaj, S., Suchard, M.A., Pybus, O.G., Lemey, P., Kraemer, M.U.G., Yu, H., 2024a. COVID-19 pandemic interventions reshaped the global dispersal of seasonal influenza viruses. Science 386. https://doi.org/10.1126/science.adq3003.

Chen, B., Tu, Y., An, J., Wu, S., Lin, C., Gong, P., 2024b. Quantification of losses in agriculture production in eastern Ukraine due to the Russia-Ukraine war. Commun. Earth Environ. 5, 336. https://doi.org/10.1038/s43247-024-01488-3.

Chinazzi, M., Davis, J.T., Ajelli, M., Gioannini, C., Litvinova, M., Merler, S., Pastore y Piontti, A., Mu, K., Rossi, L., Sun, K., Viboud, C., Xiong, X., Yu, H., Halloran, M.E., Longini, I.M., Vespignani, A., 2020. The effect of travel restrictions on the spread of the 2019 novel coronavirus (COVID-19) outbreak. Science 368, 395–400. https://doi.org/10.1126/science.aba9757.

Cortés, J., Mahecha, M.D., Reichstein, M., Myneni, R.B., Chen, C., Brenning, A., 2021. Where are global vegetation greening and browning trends significant? Geophys. Res. Lett. 48. https://doi.org/10.1029/2020GL091496 e2020GL091496.

Dang, C., Shao, Z., Huang, X., Zhuang, Q., Cheng, G., Qian, J., 2024. Global vegetation productivity increased in response to COVID-19 restrictions. Geo-spat. Inf. Sci. https://doi.org/10.1080/10095020.2023.2300842.

Didan, K., 2021. MODIS/Terra vegetation indices 16-day L3 global 1km SIN grid V061 [data set]. NASA Land Processes Distributed Active Archive Center. https://doi.org/10.5067/MODIS/MOD13A2.061.

Diffenbaugh, N.S., Field, C.B., Appel, E.A., Azevedo, I.L., Baldocchi, D.D., Burke, M., Burney, J.A., Ciais, P., Davis, S.J., Fiore, A.M., Fletcher, S.M., Hertel, T.W., Horton, D.E., Hsiang, S.M., Jackson, R.B., Jin, X., Levi, M., Lobell, D.B., McKinley, G. A., Moore, F.C., Montgomery, A., Nadeau, K.C., Pataki, D.E., Randerson, J.T., Reichstein, M., Schnell, J.L., Seneviratne, S.I., Singh, D., Steiner, A.L., Wong-Parodi, G., 2020. The COVID-19 lockdowns: a window into the earth system. Nat. Rev. Earth Environ. 1, 470–481. https://doi.org/10.1038/s43017-020-0079-1.

DiMiceli, C., Townshend, J., Carroll, M., Sohlberg, R., 2021. Evolution of the representation of global vegetation by vegetation continuous fields. Remote Sens. Environ. 254, 112271. https://doi.org/10.1016/j.rse.2020.112271.

Fakir, A.M.S., Bharati, T., 2021. Pandemic catch-22: the role of mobility restrictions and institutional inequalities in halting the spread of COVID-19. PLoS One 16, e0253348. https://doi.org/10.1371/journal.pone.0253348.

Godfree, R.C., Knerr, N., Encinas-Viso, F., Albrecht, D., Bush, D., Christine Cargill, D., Clements, M., Gueidan, C., Guja, L.K., Harwood, T., Joseph, L., Lepschi, B., Nargar, K., Schmidt-Lebuhn, A., Broadhurst, L.M., 2021. Implications of the 2019–2020 megafires for the biogeography and conservation of Australian vegetation. Nat. Commun. 12, 1023. https://doi.org/10.1038/s41467-021-21266-5.

Gomes, M.S., Cavalcanti, I.F. de A., Müller, G.V., 2021. 2019/2020 drought impacts on South America and atmospheric and oceanic influences. Weather Clim. Extremes 34, 100404. https://doi.org/10.1016/j.wace.2021.100404.

Hale, T., Angrist, N., Goldszmidt, R., Kira, B., Petherick, A., Phillips, T., Webster, S., Cameron-Blake, E., Hallas, L., Majumdar, S., Tatlow, H., 2021. A global panel database of pandemic policies (Oxford COVID-19 government response tracker). Nat. Hum. Behav. 5, 529–538. https://doi.org/10.1038/s41562-021-01079-8.

Hasell, J., Mathieu, E., Beltekian, D., Macdonald, B., Giattino, C., Ortiz-Ospina, E., Roser, M., Ritchie, H., 2020. A cross-country database of COVID-19 testing. Sci. Data 7, 1–7. https://doi.org/10.1038/s41597-020-00688-8.

Higgins, S.I., Conradi, T., Muhoko, E., 2023. Shifts in vegetation activity of terrestrial ecosystems attributable to climate trends. Nat. Geosci. 16, 147–153. https://doi.org/10.1038/s41561-022-01114-x.

Holail, S., Saleh, T., Xiao, X., Xiao, J., Xia, G.-S., Shao, Z., Wang, M., Gong, J., Li, D., 2024. Time-series satellite remote sensing reveals gradually increasing war damage in the Gaza Strip. Natl. Sci. Rev. 11, nwae304. https://doi.org/10.1093/nsr/nwae304.

Jiao, W., Wang, L., Smith, W.K., Chang, Q., Wang, H., D'Odorico, P., 2021. Observed increasing water constraint on vegetation growth over the last three decades. Nat. Commun. 12, 1–9. https://doi.org/10.1038/s41467-021-24016-9.

Kaplan, G., Rashid, T., Gasparovic, M., Pietrelli, A., Ferrara, V., 2022. Monitoring war-generated environmental security using remote sensing: a review. Land Degrad. Dev. 33, 1513–1526. https://doi.org/10.1002/ldr.4249.

Kashyap, R., Kuttippurath, J., Patel, V.K., 2023. Improved air quality leads to enhanced vegetation growth during the COVID-19 lockdown in India. Appl. Geogr. 151, 102869. https://doi.org/10.1016/j.apgeog.2022.102869.

Kennedy, C.M., Oakleaf, J.R., Theobald, D.M., Baruch-Mordo, S., Kiesecker, J., 2019. Managing the middle: a shift in conservation priorities based on the global human modification gradient. Glob. Chang. Biol. 25, 811–826. https://doi.org/10.1111/gcb.14549.

Lenharo, M., 2023. WHO declares end to COVID-19's emergency phase. Nature. https://doi.org/10.1038/d41586-023-01559-z.

Li, X., Wang, K., Huntingford, C., Zhu, Z., Peñuelas, J., Myneni, R.B., Piao, S., 2024. Vegetation greenness in 2023. Nat. Rev. Earth Environ. 5, 241–243. https://doi.org/10.1038/s43017-024-00543-z.

Manica, M., Guzzetta, G., Riccardo, F., Valenti, A., Poletti, P., Marziano, V., Trentini, F., Andrianou, X., Mateo-Urdiales, A., del Manso, M., Fabiani, M., Vescio, M.F., Spuri, M., Petrone, D., Bella, A., Iavicoli, S., Ajelli, M., Brusaferro, S., Pezzotti, P., Merler, S., 2021. Impact of tiered restrictions on human activities and the epidemiology of the second wave of COVID-19 in Italy. Nat. Commun. 121 (12), 1–9. https://doi.org/10.1038/s41467-021-24832-z.

Mathieu, E., Ritchie, H., Rodés-Guirao, L., Appel, C., Giattino, C., Hasell, J., Macdonald, B., Dattani, S., Beltekian, D., Ortiz-Ospina, E., Roser, M., 2020. Coronavirus Pandemic (COVID-19). Our World Data.

Olofsson, P., Foody, G.M., Herold, M., Stehman, S.V., Woodcock, C.E., Wulder, M.A., 2014. Good practices for estimating area and assessing accuracy of land change. Remote Sens. Environ. 148, 42–57. https://doi.org/10.1016/j.rse.2014.02.015.

Piao, S., Wang, X., Ciais, P., Zhu, B., Wang, T., Liu, J., 2011. Changes in satellite-derived vegetation growth trend in temperate and boreal Eurasia from 1982 to 2006. Glob. Chang. Biol. 17, 3228–3239. https://doi.org/10.1111/j.1365-2486.2011.02419.x.

Roy, R., Agarwal, V., 2020. Millions of indians are fleeing cities, raising fears of a coronavirus 'land mine'in villages. Wall Str. J.

Saxena, A., Dutta, A., Fischer, H.W., Keleman Saxena, A., Jantz, P., 2021. Forest livelihoods and a "green recovery" from the COVID-19 pandemic: insights and emerging research priorities from India. Forest Policy Econ. 131, 102550. https://doi.org/10.1016/j.forpol.2021.102550.

Silva Junior, C.H.L., Pessôa, A.C.M., Carvalho, N.S., Reis, J.B.C., Anderson, L.O., Aragão, L.E.O.C., 2020. The Brazilian Amazon deforestation rate in 2020 is the greatest of the decade. Nat. Ecol. Evol. 5, 144–145. https://doi.org/10.1038/s41559-020-01368-x.

Smith, T., Traxl, D., Boers, N., 2022. Empirical evidence for recent global shifts in vegetation resilience. Nat. Clim. Chang. 12, 477–484. https://doi.org/10.1038/s41558-022-01352-2.

Song, S., Yan, X., Zhang, X., Gao, Z., Xie, W., 2025. Weakened future surface warming in China due to national planned afforestation through biophysical feedback. npj Clim. Atmos. Sci. 81 (8), 1–12. https://doi.org/10.1038/s41612-025-00915-2.

Su, F., Fu, D., Yan, F., Xiao, H., Pan, T., Xiao, Y., Kang, L., Zhou, C., Meadows, M., Lyne, V., Wilson, J.P., Zhao, N., Yang, X., Liu, G., 2021. Rapid greening response of China's 2020 spring vegetation to COVID-19 restrictions: implications for climate change. Sci. Adv. 7, 8044–8069. https://doi.org/10.1126/sciadv.abe8044.

Sulyok, M., Walker, M., 2020. Community movement and COVID-19: a global study using Google's community mobility reports. Epidemiol. Infect. 148, e284. https://doi.org/10.1017/S0950268820002757.

Venter, Z.S., Barton, D.N., Chakraborty, T., Simensen, T., Singh, G., 2022. Global 10 m land use land cover datasets: a comparison of Dynamic World, World Cover and Esri Land Cover. Remote Sens. 14, 4101. https://doi.org/10.3390/rs14164101.

Zhang, S., Zhang, J., Liang, S., Liu, S., Zhou, Y., 2022. A perception of the nexus "resistance, recovery, resilience" of vegetations responded to extreme precipitation pulses in arid and semi-arid regions: a case study of the Qilian Mountains Nature Reserve, China. Sci. Total Environ. 843, 157105. https://doi.org/10.1016/j.scitotenv.2022.157105.

Zhu, Z., Piao, S., Myneni, R.B., Huang, M., Zeng, Z., Canadell, J.G., Ciais, P., Sitch, S., Friedlingstein, P., Arneth, A., Cao, C., Cheng, L., Kato, E., Koven, C., Li, Y., Lian, X., Liu, Y., Liu, R., Mao, J., Pan, Y., Peng, S., Peñuelas, J., Poulter, B., Pugh, T.A.M., Stocker, B.D., Viovy, N., Wang, X., Wang, Y., Xiao, Z., Yang, H., Zaehle, S., Zeng, N., 2016. Greening of the earth and its drivers. Nat. Clim. Chang. 6, 791–795. https://doi.org/10.1038/nclimate3004.